

NANOMATERIALS

Carbothermal shock synthesis of high-entropy-alloy nanoparticles

Yonggang Yao,^{1*} Zhenan Huang,^{2*} Pengfei Xie,^{3*} Steven D. Lacey,^{1*} Rohit Jiji Jacob,⁴ Hua Xie,¹ Fengjuan Chen,¹ Anmin Nie,² Tiancheng Pu,³ Miles Rehwoldt,⁴ Daiwei Yu,⁵ Michael R. Zachariah,⁴ Chao Wang,^{3†} Reza Shahbazian-Yassar,^{2†} Ju Li,^{5†} Liangbing Hu^{1†}

The controllable incorporation of multiple immiscible elements into a single nanoparticle merits untold scientific and technological potential, yet remains a challenge using conventional synthetic techniques. We present a general route for alloying up to eight dissimilar elements into single-phase solid-solution nanoparticles, referred to as high-entropy-alloy nanoparticles (HEA-NPs), by thermally shocking precursor metal salt mixtures loaded onto carbon supports [temperature ~ 2000 kelvin (K), 55-millisecond duration, rate of $\sim 10^5$ K per second]. We synthesized a wide range of multicomponent nanoparticles with a desired chemistry (composition), size, and phase (solid solution, phase-separated) by controlling the carbothermal shock (CTS) parameters (substrate, temperature, shock duration, and heating/cooling rate). To prove utility, we synthesized quinary HEA-NPs as ammonia oxidation catalysts with $\sim 100\%$ conversion and $>99\%$ nitrogen oxide selectivity over prolonged operations.

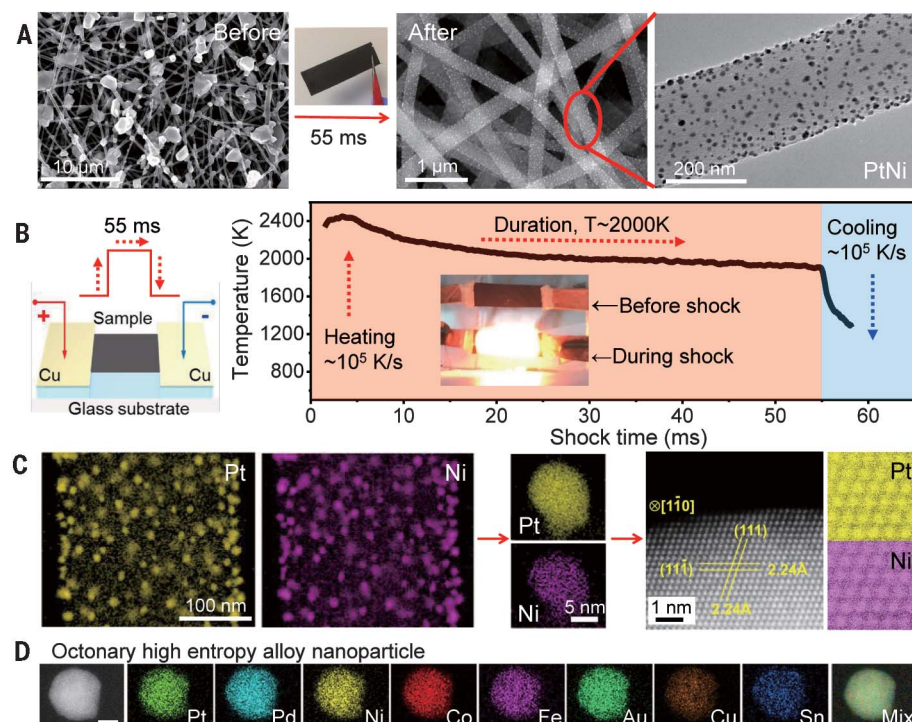
Multimetallic nanoparticles (MMNPs) are of interest in a wide range of applications, including catalysis (1–7), energy storage (8), and bio/plasmonic imaging (8, 9). Alloying multiple metallic elements into individual nanoscale products offers the promise of material properties that could exceed single-element (or unary) nanoparticles (2, 5, 6). The current and primary approaches toward the preparation of MMNPs arise from wet-chemistry synthesis, where a variety of particle sizes, shapes,

and phases can be attained (3, 4, 7, 10). However, most studies via wet-chemical methods report alloy compositions not exceeding three elements, which limits the compositional space. Additionally, more site-specific synthesis techniques, including printing- and lithography-based methods (1, 11, 12), have shifted the compositional space toward quaternary and even quinary nanostructures; however, the subsequent reduction procedures tend to limit the structural complexity to phase-separated MMNPs, especially for immiscible

elemental combinations (1, 12, 13). In terms of bulk material synthesis, melt processing is a scalable method that has led to the creation of high-entropy alloys (HEAs) consisting of five or more elements in a solid solution (uniform mixing), which have shown great potential as structural materials (14–18). To date, only a limited family of HEAs have been achieved, due to the difficulty of mixing elements with vastly different chemical and physical properties, as well as cooling rate constraints. Moreover, downsizing HEAs to the nanoscale is a daunting task, especially by conventional alloying methods. Therefore, the development of a synthesis method where elemental composition, particle size, and phase can be precisely controlled could bring about a new repertoire of alloys and nanostructures with unprecedented functionalities.

We developed a facile, two-step carbothermal shock (CTS) method that employs flash heating and cooling (temperature of ~ 2000 K, shock duration of ~ 55 ms, and ramp rates on the order of 10^5 K/s) of metal precursors on oxygenated carbon support to produce high-entropy-alloy nanoparticles (HEA-NPs) with up to eight dissimilar metallic elements (table S1). MMNPs synthesized by CTS have a narrow size distribution and are uniformly dispersed across the carbon support, despite being exposed to high temperatures that conventionally cause particle coarsening. The high temperature, in conjunction with the catalytic activities of the liquid metals, drives rapid particle “fission” and “fusion” events that result in uniform mixtures of multiple elements. Subsequently, the rapid cooling rate facilitates kinetic control over the thermodynamic mixing regimes and enables the formation of crystalline solid-solution nanoparticles, analogous to

Fig. 1. CTS synthesis of HEA-NPs on carbon supports. (A) Microscopy images of microsized precursor salt particles on the carbon nanofiber (CNF) support before thermal shock, as well as the synthesized, well-dispersed (PtNi) nanoparticles after CTS. (B) Sample preparation and the temporal evolution of temperature during the 55-ms thermal shock. (C) Low-magnification and single-particle elemental maps, an HAADF image, and corresponding atomic maps for a binary PtNi alloy. (D) Elemental maps of an HEA-NP composed of eight dissimilar elements (Pt, Pd, Ni, Co, Fe, Au, Cu, and Sn). Scale bar, 10 nm.



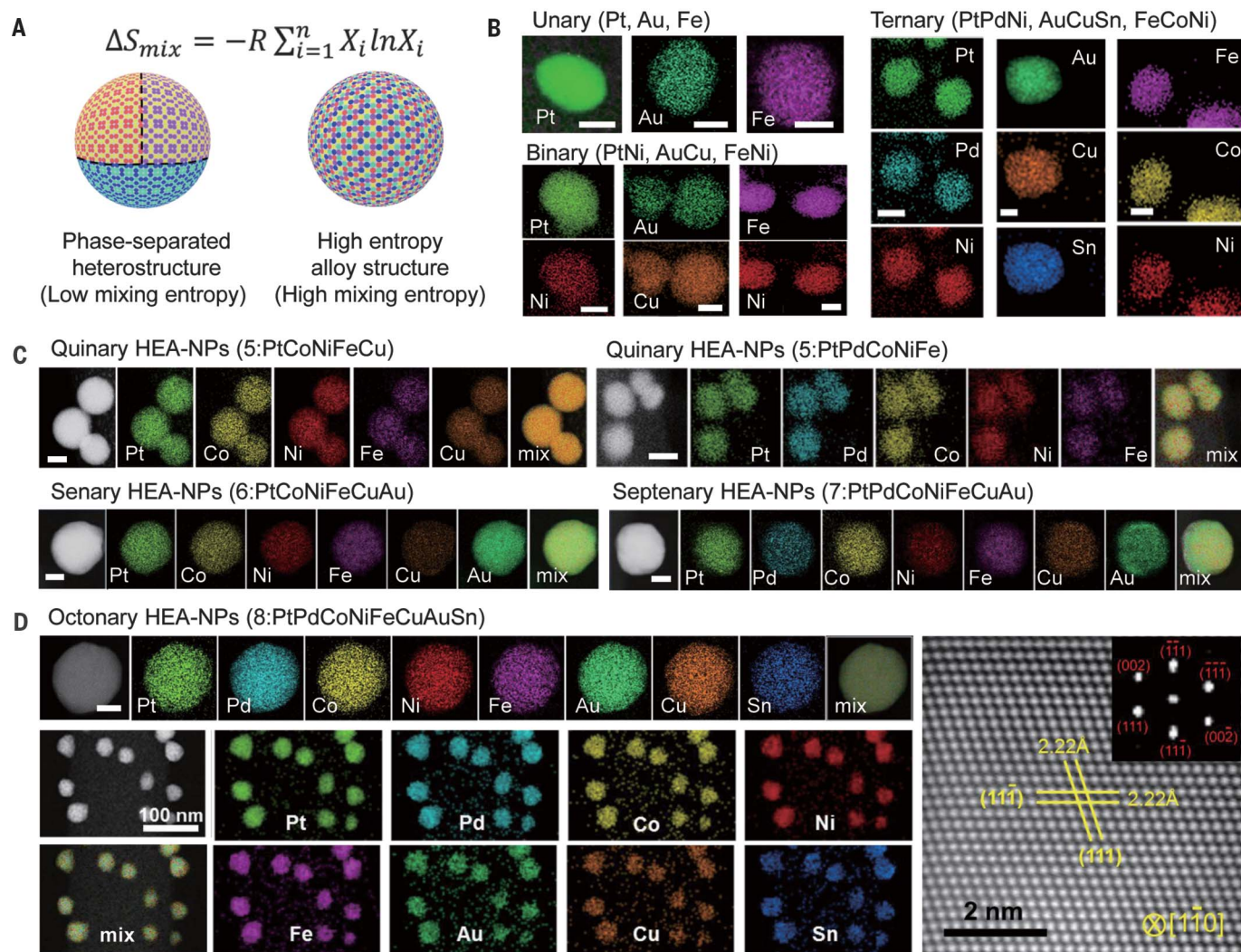


Fig. 2. Elemental characterization of HEA-NPs. (A) Schematic comparison of phase-separated heterostructures synthesized by a conventional slow reduction procedure (slow kinetics) versus solid-solution HEA-NPs synthesized by the CTS method (fast kinetics). (B) STEM elemental maps of unary (Pt, Au, and Fe), binary (PtNi, AuCu, and FeNi), and ternary (PtPdNi, AuCuSn, and FeCoNi) nanoalloys. Scale bar, 5 nm. (C) HAADF images and STEM elemental maps of HEA-NPs: quinary (PtFeCoNiCu and PtPdCoNiFe), senary (PtCoNiFeCuAu), and septenary (PtPdCoNiFeCuAu). Scale bar, 10 nm. (D) Individual and low-magnification elemental maps (left) and a high-resolution HAADF-STEM image with fast Fourier transform analysis (right) of octonary (PtPdCoNiFeCuAuSn) HEA-NPs, showing solid solutions with an fcc structure. The low-magnification elemental maps verify the structural and compositional uniformity of the HEA-NPs. Scale bar, 10 nm.

martensitic steels and metallic glasses that are also kinetically trapped (19, 20). By adjusting the input electrical pulse parameters, we can also produce phase-separated nanoparticles by decreasing the cooling rate. This CTS technique opens a

vast space for synthesizing alloys and nanocrystals, which has potential for a wide range of applications.

Results

The CTS method we used to synthesize uniformly dispersed, solid-solution nanoparticles (up to eight elements) requires two steps (21). First, we mixed metal salt precursors MCl_xH_y (M is Pt, Pd, Ni, Fe, Co, Au, Cu, or Sn, among others) into a solution and loaded onto a conductive carbon support, such as carbon nanofibers (CNFs). CNFs carbonized at 1073 K (CNF-1073K, denoted as CNF hereafter) are the substrates used in this work unless stated otherwise. After drying, we exposed the precursor-loaded sample to a rapid thermal shock (55 ms) in an Ar-filled glovebox, which leads to a high concentration of nanoparticles

(e.g., PtNi) that form across the carbon surface (Fig. 1A and figs. S1 to S4). The electrical pulse that we applied controls the thermal exposure conditions (Fig. 1B), with a common temperature of ~2000 K and heating/cooling rates up to $\sim 10^5$ K/s as measured with a pyrometer (figs. S5 to S7). We found no apparent elemental segregation or phase separation for the PtNi nanoparticles (Fig. 1C and fig. S4) using scanning transmission electron microscopy (STEM) elemental maps. The high-angle annular dark-field (HAADF) images and atomic maps also demonstrated both uniform atomic scale mixing and the formation of a face-centered cubic (fcc) crystalline structure (Fig. 1C). Our general method extends to more complex HEA-NPs. For example, we readily fabricated HEA-NPs composed of eight dissimilar elements (Pt, Pd, Ni, Co, Fe, Au, Cu, and Sn). These elements

¹Department of Materials Science and Engineering, University of Maryland, College Park, MD 20742, USA. ²Department of Mechanical and Industrial Engineering, University of Illinois at Chicago (UIC), Chicago, IL 60607, USA. ³Department of Chemical and Biomolecular Engineering, Johns Hopkins University, Baltimore, MD 21218, USA. ⁴Department of Chemical and Biomolecular Engineering and Chemistry and Biochemistry, University of Maryland, College Park, MD 20742, USA. ⁵Department of Nuclear Science and Engineering, Department of Materials Science and Engineering, and Department of Electrical Engineering and Computer Science, Massachusetts Institute of Technology, Cambridge, MA 02139, USA.

*These authors contributed equally to this work.

†Corresponding author. Email: binghu@umd.edu (L.H.); rsyassar@uic.edu (R.S.-Y.); liju@mit.edu (J.L.); chaowang@jhu.edu (C.W.)

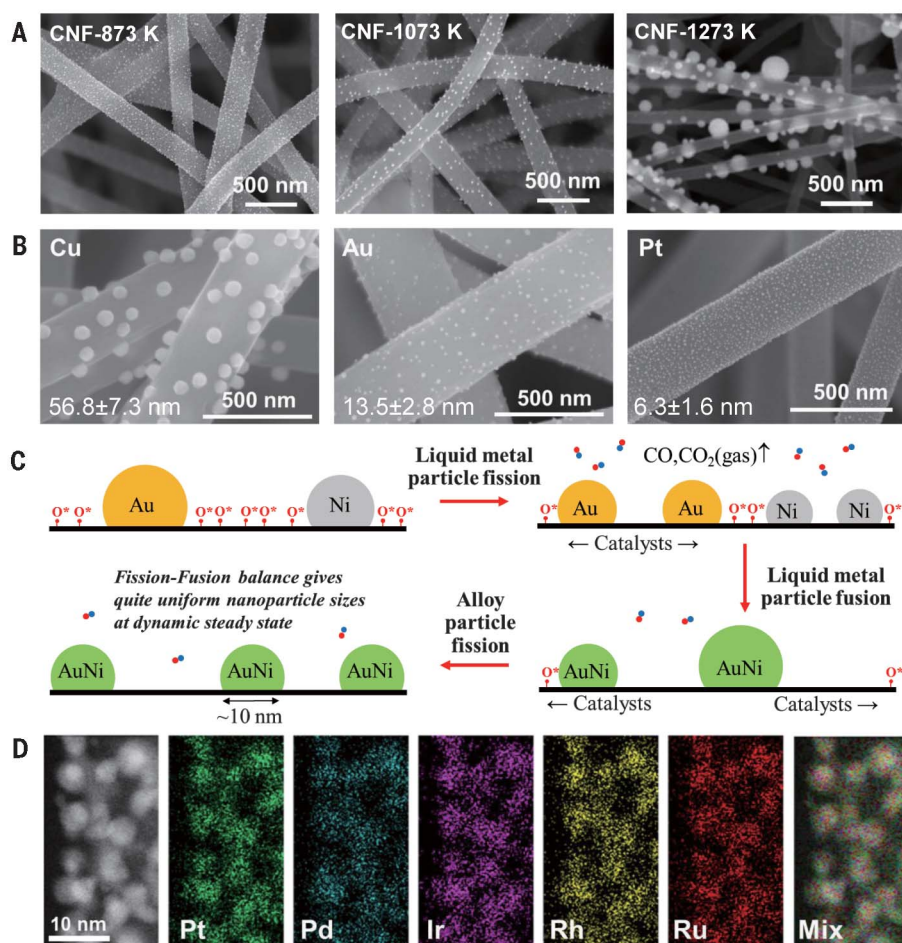


Fig. 3. Particle dispersion mechanism for the CTS process. (A) SEM images of synthesized AuNi nanoparticles on CNFs carbonized at different temperatures: 873, 1073, and 1273 K. A higher carbonization temperature leads to higher crystallinity and lower defect concentrations within the carbon support, which affects particle size and dispersion. (B) SEM images of Cu, Au, and Pt particle distributions synthesized on identical CNF supports via the same CTS process. The higher catalytic activities of the metal species (Au and Pt) lead to smaller nanoparticles and more uniform distributions. (C) An illustration of the catalysis-driven particle fission/fusion mechanism to synthesize uniformly dispersed HEA-NPs. (D) HAADF image and elemental maps of ultrafine and well-dispersed quinary HEA-NPs (PtPdIrRhRu) on CO_2 -activated CNFs. A narrow size distribution is achieved by increasing the support's surface defect concentration through CO_2 activation, as well as employing metal species with high catalytic activities.

have a range of atomic radii (1.24 to 1.44 Å), reduction potentials (−0.25 to 1.5 V versus the standard hydrogen electrode), preferred crystal structures (fcc, body-centered cubic, hexagonal close-packed, or tetragonal), and melting temperatures (500 to 2000 K) that typically prevents solid-solution formation (Fig. 1D and table S2).

MMNPs have been previously synthesized using conventional reduction procedures (1, 3). However, these synthetic methods tend to create phase-separated heterostructures among immiscible elements, which greatly reduces the configurational entropy of mixing (fig. S8). The CTS process leads to solid solution MMNPs (i.e., HEA-NPs), where arbitrary metallic elements are completely mixed to maximize the mixing entropy (ΔS_{mix}) (Fig. 2A). We demonstrated the

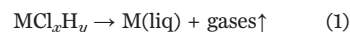
versatility by synthesizing a series of multi-element nanoparticles and characterized them by STEM, transmission EM (TEM), scanning EM (SEM), and energy-dispersive x-ray spectroscopy (EDS). We synthesized unary (Pt, Au, and Fe), binary (PtNi, AuCu, and FeNi), and ternary (PtPdNi, AuCuSn, and FeCoNi) nanoparticles that exhibit compositional uniformity (Fig. 2B). The nanoparticles also possess size uniformity, with diameters of ≥ 5 nm (fig. S9), regardless of the elemental compositions. By adding additional metal salts to the precursor solutions, we synthesized quinary (PtCoNiFeCu and PtPdCoNiFe), senary (PtCoNiFeCuAu), septenary (PtPdCoNiFeCuAu) and octonary (PtPdCoNiFeCuAuSn) HEA-NPs, which are solid solutions and evenly dispersed across the

carbon support (Fig. 2, C and D, and figs. S10 to S16). Moreover, the HEA-NPs are of nanoscale dimensions in fcc crystal structures (Fig. 2D and figs. S17 and S18).

The HEA-NPs exhibited solid solution mixing via the same 55-ms thermal shock protocol (figs. S19 and S21). We confirmed the structural uniformity (no phase separation) and negligible chlorine content with STEM (figs. S22 to S26), x-ray diffraction (XRD) (figs. S27 to S29), and x-ray photoelectron spectroscopy (XPS) (figs. S30 to S36). A statistical study conducted over different sample regions confirms the compositional uniformity among the synthesized nanoparticles (figs. S37 to S43). For example, the compositional variation for each element in our quinary HEA-NPs (PtPdCoNiFe) is $\sim 10\%$, which is smaller than the $>50\%$ variation reported for lithography-based techniques (fig. S42) (1). Additionally, the macroscopic compositions that we determined by inductively coupled plasma mass spectroscopy (ICP-MS) agree well with the STEM-derived statistics. The HEA-NP composition has a small deviation from the ideal composition based on the initial precursor salt molar ratios, due to vapor loss at high temperature (figs. S44 to S46 and table S3). To demonstrate compositional control, we employed the (precursor) compensation approach, which is a common strategy in high-temperature synthesis when volatile elements are involved (figs. S47 to S52).

The HEA-NPs deviate from the phase-separated thermodynamic equilibrium structures reported in literature (1, 3, 12) due to the rapid quench-induced nucleation/growth process of the CTS method, which “freezes” the liquid alloy state to create solid-solution nanoparticles. The synthesized HEA-NPs are stable at room temperature and remained unchanged in terms of size, structure, and composition after 11 months of storage under standard conditions.

In addition to the rich chemistries, the morphologies of the synthesized nanoparticles indicate a formation mechanism for CTS that differs from other alloying approaches. Because ~ 2000 K far exceeds the thermal decomposition temperature of metal precursors (table S1), the salts easily decompose:

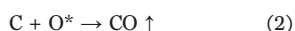


However, ~ 2000 K is below the boiling points of the metallic elements. In this case, the metallic elements are likely in the liquid phase and should be on a similar length scale as the initial (microsized) salt precursors. Since metals are nonwetting with carbon, the liquid metals should coarsen to minimize their surface energy at high temperature (22). Our observation departs from this behavior, requiring a mechanism to explain how initially single-element, micron-sized liquid metal droplets form uniformly dispersed alloy nanoparticles.

We performed two control experiments to explore HEA-NP formation. We found distinct particle morphology differences using the same CTS protocol (Fig. 3A and figs. S53 and S54), but with

supports differing in carbonization temperature. Specifically, electrospun polyacrylonitrile fibers carbonized in argon at a range of temperatures (873, 1073, and 1273 K) generated CNF supports with various defect concentrations. Lower carbonization temperatures resulted in smaller, more uniform particle dispersions. Each pyrolysis temperature was insufficient to drive away all surface-bound oxygen (O^*) and thus resulted in an increasing amount of O^* residuals remaining on CNFs carbonized at lower temperatures (fig. S2). Therefore, we surmised that the surface defect concentration of the carbon support is an important parameter for particle dispersion. Our second control experiment used identical CNF supports (CNF-1073K) and synthesis conditions (55 ms, ~ 2000 K), but with a variety of single-metal salt precursors (Fig. 3B and figs. S55 to S57). Nanoparticle size distribution changes in this case with Cu having a much larger particle size (~ 56.8 nm) than Au (~ 13.5 nm) and Pt (~ 6.3 nm). This trend resembles the catalytic activities of the corresponding elements, with Pt and Cu being the most and least active, respectively. Because Au and Cu possess similar physical properties (table S4), the discrepancy requires a different particle dispersion mechanism than a simple, physical melting-and-nucleation process.

Since defects and metal catalysts play a key role during the CTS process, we considered a catalytically driven particle dispersion mechanism for the defective carbon supports. To verify this, we used in situ mass spectrometry to analyze the gases created during CTS for defective CNF supports with and without precursor salts. Compared with bare CNF, the precursor-loaded CNF exhibited a larger and much sharper release of CO gas during the CTS process (fig. S58). Thus, the release of CO gas upon thermal shock arises from a catalytically driven carbon metabolism reaction:



where O^* denotes surface-bound residual oxygen. The carbon metabolism reaction involves C (fuel), O^* (oxidizer), and metal (catalyst), which correlates the surface defect concentration (e.g., carbonization temperature) and the metal's catalytic activity to the final nanoparticle size and level of dispersity. We hypothesize that during the 55-ms high-temperature exposure, the liquid metal droplets actively travel around and split ("fission") to harvest the dispersed O^* on the carbon surface based on the catalytically driven reaction, $C + O^* = CO$ (gas) ($\Delta H = -110.5$ kJ/mol). Previously published works (23–26) and an in situ TEM study (27) also showed that metallic particles can move and split under a catalytic driving force, which is similar to our proposed carbon metabolism reaction.

Mechanistically (Fig. 3C), a larger O^* concentration and the use of catalytically active metals can drive vigorous metabolism with more frequent catalyst motion and fission events. This opposes equilibrium thermodynamic directive for the metal droplets to coarsen. Conversely,

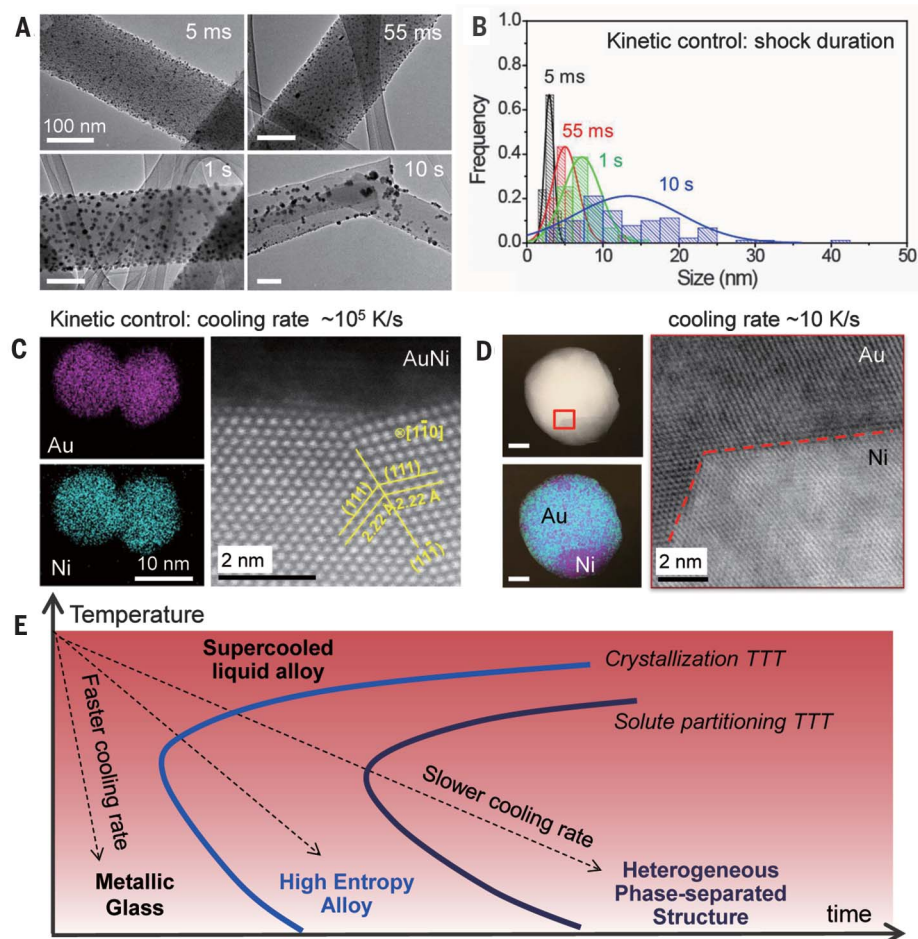


Fig. 4. Kinetic control over nanoparticle formation. (A) TEM images displaying the particle size and dispersity at various thermal shock durations (5 ms, 55 ms, 1 s, and 10 s). Scale bars, 100 nm. (B) Particle size distribution of PtNi nanoparticles on CNFs. (C and D) Cooling rate-dependent AuNi nanostructures determined by elemental maps, HAADF, and ABF images. Ultrafast cooling rates ($\sim 10^5$ K/s) enable the formation of solid-solution nanoparticles, whereas slower rates (~ 10 K/s) tend to induce phase separation. Scale bar, 10 nm. (E) Time-temperature-transformation (TTT) diagram showing the kinetic formation of metallic glass, HEA, and phase-separated structures, respectively, as a function of cooling rate.

depleted O^* concentrations should lead to decreased mobility and the localization of liquid droplets that coarsen slowly to reduce their total surface energy. The liquid alloys have a wide solubility range at ~ 2000 K. Therefore, the liquid metal movement driven by O^* harvesting allows different droplet compositions to continually meet and fuse into single-phase alloys during the CTS process. Numerous particle fusion and fission events, which we estimated to be $>10^6$ times based on time-scale analysis (fig. S59) (28–30), yield a dynamic steady state during the 55-ms high-temperature shock. This enables uniform nanoscale dispersions and homogeneous high-entropy mixing. To verify the effects of supports with more surface-bound defects, we synthesized quinary HEA-NPs (PtFeCoNiCu) on CNFs with and without CO_2 activation, resulting in 5.30 ± 1.31 -nm particles on CO_2 -activated CNFs and 11.3 ± 2.2 -nm particles on CNFs (fig. S60). We achieved further improvements in

ultrafine particle sizes and narrow distributions when more catalytically active metal combinations (PtPdIrRhRu HEA-NPs, 3.28 ± 0.81 nm) are employed on identical CO_2 -activated CNF supports (Fig. 3D and figs. S61 and S62). Therefore, the catalytic metabolism-induced particle fission/fusion mechanism for metal alloying at the nanoscale is distinct compared with previously reported alloying methods (1, 3, 7, 16).

By tuning the shock duration and heating/cooling rates, we can adjust the MMNP size, distribution, and structure. We loaded multiple CNF samples using an identical PtNi precursor solution and exposed the support to a temperature of ~ 2000 K for 5-ms, 55-ms, 1-s, and 10-s durations. The faster exposure times yield smaller particle sizes (3.51 ± 0.62 nm for 5 ms and 5.01 ± 1.69 nm for 55 ms) compared with prolonged shock durations (8.57 ± 1.98 nm for 1 s and 13.30 ± 6.98 nm for 10 s) (Fig. 4, A and B). We observed similar behavior with AuNi (fig. S63). As the thermal shock

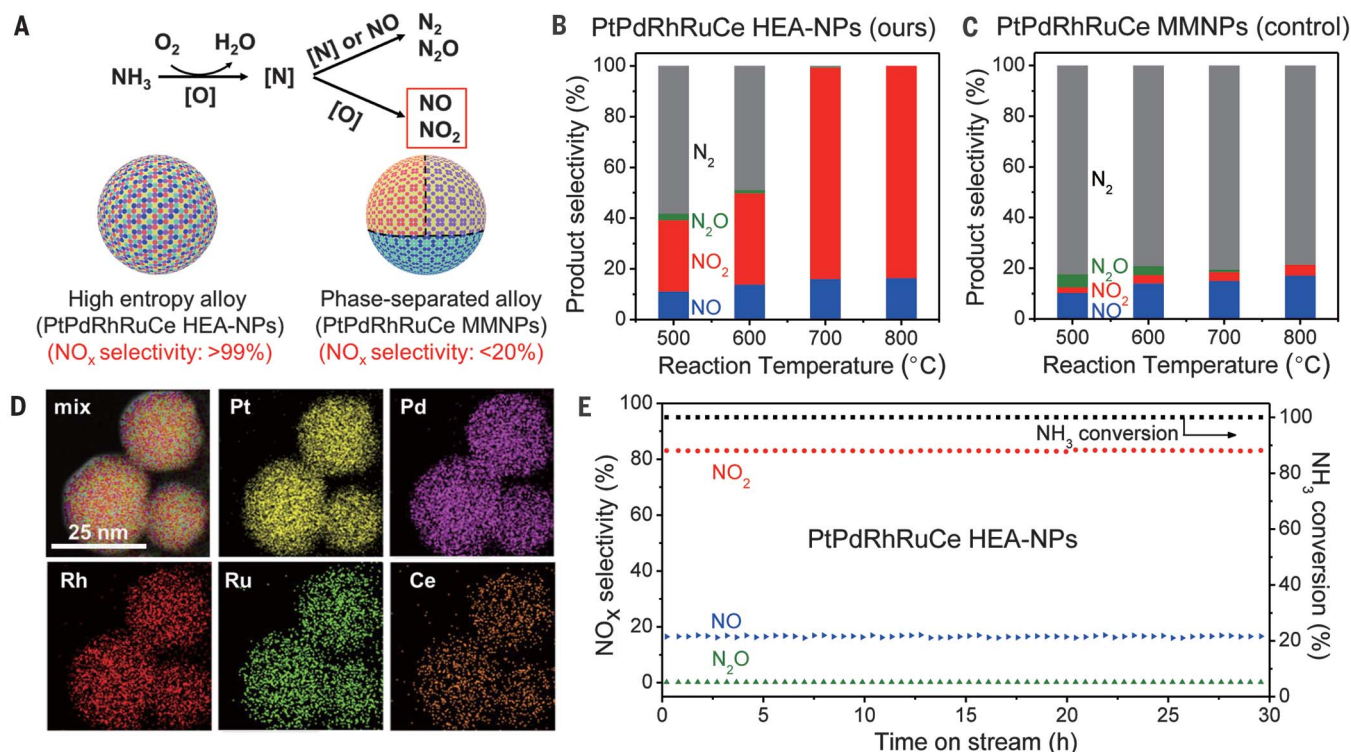


Fig. 5. Catalytic performance of quinary HEA-NPs (PtPdRhRuCe) for ammonia oxidation. (A) Reaction scheme for the ammonia oxidation process as well as the structural and performance differences between the PtPdRhRuCe HEA-NPs synthesized by CTS and the control sample (PtPdRhRuCe MMNPs) by wet impregnation.

duration increases to 10 s, the size of the HEA-NPs increases and the synthesized particles become less uniform; the high-temperature exposure depletes the number of O* present on the CNF support, which inhibits particle fission and corresponding dispersity (fig. S64).

We investigated the effect of cooling rate by tuning the electrical input parameters (Fig. 1B) with Au/Ni and Cu/Co, which are immiscible binary elemental compositions (Fig. 4, C and D, and figs. S65 to S67). Due to differences in lattice parameters and surface energies, these metallic combinations tend to phase-separate according to equilibrium phase diagrams (3, 20, 31). However, through rapid quenching, the high-entropy mixing state of the liquid metals is retained and yields single-phase solid-solution nanoparticles (i.e., HEA-NPs) by avoiding the time-temperature-transformation (TTT) nose (Fig. 4E). The AuNi binary alloy formed a solid solution when quenched at both $\sim 10^5$ and $\sim 10^3$ K/s (Fig. 4C and fig. S66). However, nanoscale phase separation occurred when cooled slowly (~ 10 K/s), with a clear phase boundary between Au and Ni shown in the annular bright-field (ABF) image (Fig. 4D) and HAADF image (fig. S66). For the CuCo binary system, the 10^5 K/s produced a solid solution, but phase separation began at a cooling rate of $\sim 10^3$ K/s (fig. S65). Very slow cooling and heating rates (~ 10 K/s) also alter the dispersion and size distribution of the synthesized nanoparticles, which leads to

aggregates and a nonuniform particle dispersion across the CNFs (figs. S67 and S68).

Our experimental results reveal valuable information about the nucleation and diffusion kinetics of the CTS method. The transformation of a liquid alloy into a single-phase solid solution with a specific elemental composition requires local structural rearrangements but no long-range solute partitioning. The cooling rate ($\sim 10^5$ K/s) that we achieved by CTS is still slow enough to form crystalline structures. If higher cooling rates are attained with the CTS method, it may be possible to use this route to synthesize metallic glasses. The $\sim 10^5$ K/s cooling rate is fast enough to prevent solute partitioning across a distance of ~ 10 nm, enabling the formation of high-entropy-alloy structures. On the other hand, slower cooling rates (e.g., ~ 10 K/s) enable solute partitioning to occur through (slow) kinetics, which caused the MMNPs to phase separate into a Janus particle. Both single-phase and phase-separated nanoparticles are useful for applications such as catalysis and plasmonic imaging (2, 3, 9, 10). The CTS method has the ability to control phase formation through ramp rates and may be useful for targeted nanoparticle synthesis.

The CTS method enables diverse compositions of uniformly mixed HEA-NPs that have potential for a wide range of applications. As a proof of concept, we demonstrated quinary HEA-NPs as advanced catalysts for ammonia oxidation, which

is the key processing step in the industrial synthesis of nitric acid (Fig. 5A) (32). Despite extensive efforts on the exploration of new catalysts, PtPdRh-based multimetallic catalysts are still widely employed in industry to this day (33). Beyond the high content of precious metals, these catalysts also require very high temperatures ($>800^\circ\text{C}$) to achieve high yields of NO_x (NO + NO₂) versus N₂/N₂O and tend to degrade under continuous operation (34). Using the CTS method, quinary PtPdRhRuCe HEA-NPs (figs. S69 and S70 and table S5 for the compositions) were prepared and employed as ammonia oxidation catalysts (2). We introduced Ru and Ce to improve the overall catalytic activity and reduce the Pt content (35, 36).

We achieved $\sim 100\%$ conversion of ammonia (NH₃) and $>99\%$ selectivity toward NO_x (NO + NO₂) at a relatively low operation temperature of 700°C with the PtPdRhRuCe HEA-NP catalyst (Fig. 5B). For comparison, we prepared similar catalysts (in terms of composition) by the wet impregnation method (denoted as PtPdRhRuCe MMNPs), which produced a 18.7% yield of NO_x at the same operation temperature, whereas most of the output was N₂ (Fig. 5C). An elemental map comparison between the two catalysts suggests that the enhanced catalytic selectivity of the HEA-NPs is likely due to the highly homogeneous nature of the solid-solution nanoparticles compared with the phase-separated heterostructures derived from the wet impregnation method

(Fig. 5D and fig. S70). Note that synthesizing solid-solution PtPdRh multimetallic systems by conventional synthetic methods is challenging due to immiscibility (2, 34). We also performed degradation testing to study catalytic performance under prolonged operation conditions, and we observe no degradation in terms of catalytic activity or selectivity over ~30 hours of continuous operation at 700°C (Fig. 5E and fig. S71). We attributed this durability to the high-entropy nature of the catalysts prepared by the CTS method, which helps stabilize the MMNPs in solid solutions (i.e., HEA-NPs) and prevents phase separation or elemental segregation under the reaction conditions (16, 18). Moreover, the precious metal content of the HEA-NPs can be reduced further without compromising catalytic performance or stability by replacing ~37.5% of Pt with Co and eliminating Ru (e.g., PtPdRhCoCe HEA-NPs) (fig. S72). Thus, HEA-NPs fabricated by the CTS method may be a general route toward highly active, durable, and cost-effective catalysts (see table S6 for a detailed literature comparison).

Discussion and conclusion

The CTS method provides an excellent platform for nanometallurgical studies. Immiscible elements are alloyed into single-phase nanoparticles on carbon supports with the following features: (i) high-entropy mixing, where multimetallic mixing leads to the creation of solid-solution nanoparticles with maximized configurational mixing entropy; (ii) nonequilibrium processing, where the shock process takes milliseconds to create HEA-NPs by rapid quenching and thus prevents phase separation among immiscible elements by avoiding the nose of the TTT curve (Fig. 4E); and (iii) uniform dispersion, where the catalytically driven carbon metabolism at high temperature enables uniform, well-dispersed, and controllably sized nanoparticles (as opposed to particle coarsening).

This synthetic technique also provides (i) generality, (ii) tunability, and (iii) potential scalability. The maximum temperature of the CTS method (2000 to 3000 K) is higher than the decomposition temperature of any metal salt, which promotes uniform mixing of nearly any metallic combination (i.e., generality). Precise control over the shock parameters (temperature, duration, and

ramp rates) effectively tunes the particle size, dispersity, as well as final structure. The synthesis of a diverse array of nanoparticles with easily tunable processing parameters is ideal for large-scale nanomanufacturing, where a rapid (synthesis in milliseconds) and energy-efficient (immediate heating through an electrical pulse) synthetic procedure could enable high-rate and high-volume production of quality nanoparticles. Moreover, a scalability evaluation exhibited a 100-fold increase in HEA-NP production without sacrificing nanoparticle quality or dispersion by employing a three-dimensional carbon support (figs. S73 to S75). These CTS capabilities facilitate a new research area for materials discovery and optimization, where the elemental composition and mixing entropy of nanoparticles can be carefully designed and controlled. Further compositional exploration has the potential to transcend research efforts to broad technological applications.

REFERENCES AND NOTES

- P.-C. Chen *et al.*, *Science* **352**, 1565–1569 (2016).
- L. Bu *et al.*, *Science* **354**, 1410–1414 (2016).
- S. G. Kwon *et al.*, *Nat. Mater.* **14**, 215–223 (2015).
- M. Takahashi *et al.*, *Sci. Adv.* **3**, e1700101 (2017).
- X. Huang *et al.*, *Science* **348**, 1230–1234 (2015).
- G. Chen *et al.*, *Science* **344**, 495–499 (2014).
- M. R. Buck, J. F. Bondi, R. E. Schaak, *Nat. Chem.* **4**, 37–44 (2011).
- N. A. Frey, S. Peng, K. Cheng, S. Sun, *Chem. Soc. Rev.* **38**, 2532–2542 (2009).
- M. B. Cortie, A. M. McDonagh, *Chem. Rev.* **111**, 3713–3735 (2011).
- K. D. Gilroy, A. Ruditskiy, H.-C. Peng, D. Qin, Y. Xia, *Chem. Rev.* **116**, 10414–10472 (2016).
- E. Reddington *et al.*, *Science* **280**, 1735–1737 (1998).
- P. C. Chen *et al.*, *J. Am. Chem. Soc.* **137**, 9167–9173 (2015).
- P.-C. Chen *et al.*, *J. Am. Chem. Soc.* **139**, 9876–9884 (2017).
- S. Ranganathan, *Curr. Sci.* **85**, 1404–1406 (2003).
- J.-W. Yeh *et al.*, *Adv. Eng. Mater.* **6**, 299–303 (2004).
- B. S. Murty, J.-W. Yeh, S. Ranganathan, *High-Entropy Alloys* (Butterworth-Heinemann, 2014).
- Z. Li, K. G. Pradeep, Y. Deng, D. Raabe, C. C. Tasan, *Nature* **534**, 227–230 (2016).
- Y. F. Ye, Q. Wang, J. Lu, C. T. Liu, Y. Yang, *Mater. Today* **19**, 349–362 (2016).
- D. C. Hofmann *et al.*, *Nature* **451**, 1085–1089 (2008).
- D. A. Porter, K. E. Easterling, M. Y. Sherif, *Phase Transformations in Metals and Alloys* (CRC Press, ed. 3, 2009).
- Materials and methods are available as supplementary materials.
- N. Eustathopoulos, M. G. Nicholas, B. B. Drevet, *Wettability at High Temperatures* (Elsevier, 1999), vol. 3.
- M. Lukas *et al.*, *Nat. Commun.* **4**, 1379 (2013).
- F. Tao *et al.*, *Science* **322**, 932–934 (2008).
- M. A. Newton, C. Belver-Coldeira, A. Martínez-Arias, M. Fernández-García, *Nat. Mater.* **6**, 528–532 (2007).
- F. Tao *et al.*, *Science* **327**, 850–853 (2010).
- P.-H. Lu *et al.*, arXiv:1802.00207 [physics.app-ph] (1 Feb 2018).
- N. Combe, P. Jensen, A. Pimpinelli, *Phys. Rev. Lett.* **85**, 110–113 (2000).
- C. C. Wang *et al.*, *Nano Res.* **8**, 2143–2151 (2015).
- D.-G. Xie *et al.*, *Nat. Mater.* **14**, 899–903 (2015).
- D. Wang, Y. Li, *J. Am. Chem. Soc.* **132**, 6280–6281 (2010).
- D. M. Considine, *Chemical and Process Technology Encyclopedia* (CRC Press, 1974).
- L. Xin, H. Yongqiang, J. Husheng, *Rare Met. Mater. Eng.* **46**, 339–343 (2017).
- P. A. J. Bagot *et al.*, *J. Phys. Chem. C* **118**, 26130–26138 (2014).
- B. V. I. Chernyshev, I. M. Kisil, *Platin. Met. Rev.* **37**, 136–143 (1993).
- X. Hu, Y. Ning, L. Chen, Q. Shi, C. Jia, *Platin. Met. Rev.* **56**, 40–46 (2012).

ACKNOWLEDGMENTS

The authors thank K. Gaskell and S. Xu, as well as B. Liu, for their help with XPS and XRD measurements/analysis, respectively. The authors acknowledge the use and support of the Maryland NanoCenter and its AIMLab. This work made use of the JEOL JEM-ARM200CF in the Electron Microscopy Service (Research Resources Center, UIUC). **Funding:** This work has no direct funding support. The acquisition of the UIUC JEOL JEM-ARM200CF was supported by a MRI-R2 grant from the National Science Foundation (NSF) (DMR-0959470). R.S.Y. and J.L. acknowledge financial support from NSF DMR-1620901 and NSF DMR-1410636, respectively. S.D.L. acknowledges support by the Department of Defense through the National Defense Science and Engineering Graduate Fellowship. M.R.Z. and R.J.J. were partially supported by an Office of Naval Research Multidisciplinary University Research Initiative grant. P.X. and C.W. acknowledge the Catalytic and Discovery Awards of Johns Hopkins University. **Author contributions:** L.H. and Y.Y. conceived the idea and designed the present work. Y.Y., S.D.L., H.X., and F.C. carried out the experiments. Z.H., A.N., and R.S.Y. performed detailed microscopic characterizations. P.X., T.P., and C.W. performed high-temperature characterization and in situ molecular beam measurements. D.Y. and J.L. developed the mechanism analysis. All authors discussed the results and contributed to the final manuscript. **Competing interests:** The authors declare no competing interests. Provisional patent applications have been applied for through the University of Maryland (62523646 and 62591638). **Data and materials availability:** All data are available in the manuscript and the supplementary materials.

SUPPLEMENTARY MATERIALS

www.sciencemag.org/content/359/6383/1489/suppl/DC1
Materials and Methods
Supplementary Text
Figs. S1 to S75
Tables S1 to S6
References (37–47)

28 April 2017; resubmitted 14 December 2017
Accepted 2 February 2018
10.1126/science.aan5412

Carbothermal shock synthesis of high-entropy-alloy nanoparticles

Yonggang Yao, Zhennan Huang, Pengfei Xie, Steven D. Lacey, Rohit Jiji Jacob, Hua Xie, Fengjuan Chen, Anmin Nie, Tiancheng Pu, Miles Rehwoldt, Daiwei Yu, Michael R. Zachariah, Chao Wang, Reza Shahbazian-Yassar, Ju Li and Liangbing Hu

Science **359** (6383), 1489-1494.
DOI: 10.1126/science.aan5412

Nanoparticle synthesis gets a shock

Nanoparticles are useful in a wide range of applications such as catalysis, imaging, and energy storage. Yao *et al.* developed a method for making nanoparticles with up to eight different elements (see the Perspective by Skrabalak). The method relies on shocking metal salt-covered carbon nanofibers, followed by rapid quenching. The "carbothermal shock synthesis" can be tuned to select for nanoparticle size as well. The authors successfully created PtPdRhRuCe nanoparticles to catalyze ammonia oxidation.

Science, this issue p. 1489; see also p. 1467

ARTICLE TOOLS

<http://science.sciencemag.org/content/359/6383/1489>

SUPPLEMENTARY MATERIALS

<http://science.sciencemag.org/content/suppl/2018/03/28/359.6383.1489.DC1>

RELATED CONTENT

<http://science.sciencemag.org/content/sci/359/6383/1467.full>

REFERENCES

This article cites 41 articles, 9 of which you can access for free
<http://science.sciencemag.org/content/359/6383/1489#BIBL>

PERMISSIONS

<http://www.sciencemag.org/help/reprints-and-permissions>

Use of this article is subject to the [Terms of Service](#)